

## RESEARCH ARTICLE

10.1002/2017JC012947

## Key Points:

- Propagation of flexural gravity waves controlled by the ice-shelf/cavity system geometry
- Flexural gravity waves propagate as beams
- Flexural stresses contribute to formation and propagation of fractures and crevasses through ice shelves

## Correspondence to:

O. V. Sergienko,  
osergien@princeton.edu

## Citation:

Sergienko, O. V. (2017), Behavior of flexural gravity waves on ice shelves: Application to the Ross Ice Shelf, *J. Geophys. Res. Oceans*, 122, 6147–6164, doi:10.1002/2017JC012947.

Received 31 MAR 2017

Accepted 6 JUL 2017

Accepted article online 10 JUL 2017

Published online 1 AUG 2017

## Behavior of flexural gravity waves on ice shelves: Application to the Ross Ice Shelf

O. V. Sergienko<sup>1</sup> 
<sup>1</sup>GFDL/AOS Princeton University, Princeton, New Jersey, USA

**Abstract** Ocean waves continuously impact floating ice shelves and affect their stress regime. Low-frequency, long-period (75–400 s), ocean waves are able to reach ice-shelf cavities from distant sources and excite flexural gravity waves that represent coupled motion in the water of the cavity and the ice covering above. Analytic treatment of simplified geometric configuration and three-dimensional numerical simulations of these flexural gravity waves applied to the Ross Ice Shelf show that propagation and ice-shelf flexural stresses are strongly controlled by the geometry of the system, bathymetry of the ice-shelf cavity, and ice-shelf cavity thickness. The derived dispersion relationships, group and phase velocities of these waves can be used to infer poorly constrained characteristics of ice shelves from field observations. The results of numerical simulations show that the flexural gravity waves propagate as beams. The orientation of these beams is determined by the direction of the open ocean waves incident on the ice-shelf front. The higher frequency ocean waves cause larger flexural stresses, while lower frequency waves can propagate farther away from the ice-shelf front and cause flexural stresses in the vicinity of the grounding line.

## 1. Introduction

Being in contact with the surrounding oceans, ice shelves, floating glaciers, and ice tongues are subject to the continuous mechanical impact of ocean waves. The waves affecting ice shelves and floating glaciers range from high-frequency (short wavelength) wind-generated waves formed in the shallow seas near the ice shelves to low-frequency (long wavelength) sea swell formed by large storms and cyclones in distant oceans that travel around the globe [MacAyeal *et al.*, 2006]. As these waves reach floating ice, they induce its flexure, hence cause deformation and internal stresses that add to background viscous deformation and stress that governs the steady background flow of an ice shelf [e.g., Van der Veen, 1999]. These additional stresses potentially cause ice fracturing, formation of new, and developing already existing, crevasses, and eventually iceberg calving.

A large body of studies (using in situ and remote sensing observations) have focused on the interactions of tides with ice shelves [e.g., Stephenson, 1984; Vaughan, 1995; Shepherd and Peacock, 2003]. Among numerous tidal effects, tidally induced ice-shelf flexure at the grounding line is used as one of the indicators to determine the location of the Antarctic grounding line [e.g., Brunt *et al.*, 2010]. Investigating the effects of a short-period sea swell (10–100 s), Holdsworth and Glynn [1978, 1981] proposed that it contributes to formation of icebergs by exciting eigenmode vibrations of floating tongues. They proposed that the sea-swell frequencies are resonant with the corresponding eigenfrequencies of the floating tongues. With development of new observational techniques, more field studies are focusing on the ice-shelf/ocean-wave interactions. In situ GPSs and passive broadband seismometer measurements [MacAyeal *et al.*, 2006; Cathles *et al.*, 2009; Brunt and MacAyeal, 2014; Bromirski *et al.*, 2015] suggest that ocean waves produce a “noticeable” (i.e., detectable by instruments) impact on ice shelves. A characteristic feature of these data is high energy density in the low-frequency band [e.g., MacAyeal *et al.*, 2006; Bromirski *et al.*, 2010, 2015]. Such low-frequency waves (50–400 s) are known as infragravity (IG) waves that are formed as a result of nonlinear wave interactions along coasts [e.g., Longuet-Higgins and Stewart, 1962]. To get a basic understanding of the observed phenomena, Sergienko [2010] has used an idealized geometry of an ice shelf with uniform thickness and subice-shelf cavity with uniform depth to consider propagation of flexural gravity waves excited by such waves. The results of this simple treatment suggest that the geometric aspects (i.e., the ice-shelf thickness, the water depth, and the length of the incident waves) determine the magnitude of the wave-induced stresses.

The majority of previous studies investigating various aspects of the ice-shelf/ocean-wave interactions employ a simple geometry similar to one considered by *Sergienko* [2010]—an ice shelf with uniform thickness and its cavity with uniform water-column depth [e.g., *Sergienko*, 2013; *Godin and Zabolotin*, 2016]. In contrast to these previous studies, this study focuses on the role of the variations of the ice-shelf thickness and subice-shelf cavity depth, and explores the effects of a spatially variable geometry of an ice shelf and its subice-shelf cavity on the propagation of flexural gravity waves through the ice-shelf/subice-shelf cavity system and resulting flexural stresses in the ice shelf. The study uses two approaches. The first considers a one-dimensional configuration of the ice shelf and its cavity with slowly varying ice thickness and the water-column depth. It uses a simplified, vertically integrated treatment of the ice-shelf deformation in order to establish the characteristics of flexural gravity waves (e.g., the dispersion relationship) and flexural stresses, and their dependence on the parameters of the system and incident ocean waves. The second approach considers a three-dimensional system of an ice-shelf and subice-shelf cavity. It uses a three-dimensional numerical model of ice-shelf flexure coupled to a linear wave model applied to the geometry of the Ross Ice Shelf (RIS) and its cavity to simulate propagation of flexural gravity waves and compute their characteristics and corresponding flexural stresses. This approach is motivated by observations from a network of broadband seismometers operated on the Ross Ice Shelf (RIS) [*Bromirski et al.*, 2015].

The paper is organized as follows. It starts with the description of coupled models of ice-shelf deformation and wave propagation. This is followed by a description of a simplified, one-dimensional treatment of wave-induced flexure of an ice shelf with slowly varying ice thickness and cavity-water depth. The next section presents the results of numerical simulations of the interactions of the Ross Ice Shelf with long-period waves. The results are summarized in the last section.

## 2. Model

A model simulating ice-shelf/ocean-wave interactions consists of two components—an ice-shelf deformation model and a subice-shelf wave propagation model—coupled to each other. Ice-shelf deformations are assumed to be elastic. The choice of ice rheology is determined by characteristic timescale of ocean wave propagations through an ice-shelf cavity ( $\sim 3\text{--}6$  h depending on the size of the cavity and the wavelength of the flexural gravity wave), which are small compared to the characteristic Maxwell time [*Maxwell*, 1867] of ice, which is on the order of days to weeks [e.g., *MacAyeal and Sergienko*, 2013]. A description of the wave propagation in the ice-shelf cavity is based on potential flow theory [e.g., *Stoker*, 1957]. The two models are coupled through the additional pressure at the ice-shelf/sea-water interface created by waves and normal components of the water velocities. The coupled model is a three-dimensional version of a model described by *Sergienko* [2010], it describes propagation of flexural gravity waves through the ice-shelf/subice-shelf cavity system.

### 2.1. Ice-Shelf Deformation Model

The ice-shelf conservation of momentum is expressed by

$$\rho \frac{\partial^2 \vec{U}}{\partial t^2} = \nabla \cdot \boldsymbol{\sigma} + \rho \vec{g}, \quad (1)$$

where  $\rho$  is the ice density ( $917 \text{ kg m}^{-3}$ ),  $\vec{U} = \{u, v, w\}$  is the displacement vector,  $\nabla \cdot$  is the divergence operator,  $\boldsymbol{\sigma}$  is the stress tensor, and  $\vec{g}$  is the acceleration due to the gravity. As stated above, ice rheology is assumed to be elastic, and is described by Hooke's law [e.g., see *Timoshenko and Goodier*, 1970, p. 11]

$$\sigma_{ik} = \frac{E}{1+\nu} \left( \epsilon_{ik} + \frac{\nu}{1-2\nu} \epsilon_{ll} \delta_{ik} \right), \quad (2)$$

where  $\epsilon_{ik}$  are strains,  $E$  is Young's modulus (8.8 GPa),  $\nu$  is Poisson's ratio (0.3),  $\delta_{ik}$  is the Kronecker delta, and indices  $i$  and  $k$  refer to the components of a Cartesian coordinate system. The strain tensor is defined by

$$\epsilon_{ik} = \frac{1}{2} \left( \frac{\partial U_i}{\partial x_k} + \frac{\partial U_k}{\partial x_i} \right), \quad (3)$$

where  $U_i$  is the  $i$ th component of the displacement vector  $\vec{U}$ .

Similar to considerations of *Sergienko* [2010], the acceleration term on the left-hand side of equation (1) is assumed to be negligible compared to the terms on its right-hand side (discussed below).

## 2.2. Subice-Shelf Wave Propagation Model

Wave propagation in the ice-shelf cavity is based on potential flow theory [e.g., *Stoker*, 1957]. It is assumed that the water is inviscid and irrotational. The latter assumption is justified by the fact that the Rossby radius of deformation  $L_d = \frac{\sqrt{gH}}{f}$  (where  $H$  is a characteristic water depth,  $f$  is the Coriolis parameter) is much larger than the characteristic length of the gravity waves ( $L_d \sim 500$  km versus  $L_g \lesssim 10$  km). Under such assumptions, the flow can be described by a velocity potential  $\Phi$  such that

$$\vec{v} = \vec{\nabla} \Phi, \quad (4)$$

where  $\vec{v}$  is the water velocity.

Conservation of the sea-water mass is expressed by

$$\vec{\nabla} \cdot \vec{v} \equiv \nabla^2 \Phi = 0, \quad (5)$$

which represents the governing equation for  $\Phi$ .

## 2.3. Boundary Conditions

Ice-shelf displacements are anticipated to be small compared to its geometric dimensions, and the boundary conditions are applied at undeformed surfaces. The ice-shelf top surface,  $z = S(x, y)$ , is assumed to be traction-free, i.e.,

$$\sigma \cdot \vec{n} = 0, \quad (6)$$

where  $\vec{n}$  is an outward pointing normal unit vector. At the ice-shelf base,  $z = B(x, y)$ , the normal stress is prescribed, and the shear stress is zero

$$\sigma \cdot \vec{n} = -\vec{n} \left[ \rho_w g \left( H_i \frac{\rho}{\rho_w} - w_b \right) + p_w \right] \quad (7a)$$

$$\sigma \cdot \vec{n} - \vec{n} \cdot \sigma \cdot \vec{n} = 0, \quad (7b)$$

where  $\rho_w$  is the sea-water density ( $1028 \text{ kg m}^{-3}$ ),  $H_i(x, y)$  is the ice-shelf thickness and  $p_w$  is

$$p_w = -\rho_w \frac{\partial \Phi}{\partial t}. \quad (8)$$

Conditions at the ice-shelf front are similar to those expressed above, i.e., the normal stress is prescribed and the shear stress is zero

$$\sigma \cdot \vec{n} = \vec{n} \begin{cases} 0 & H_i \frac{\rho}{\rho_w} \leq z < H_i \\ \rho_w g \left( H_i \frac{\rho}{\rho_w} - z \right) + p_w & 0 \leq z < H_i \frac{\rho}{\rho_w} \end{cases} \quad (9a)$$

$$\sigma \cdot \vec{n} - \vec{n} \cdot \sigma \cdot \vec{n} = 0. \quad (9b)$$

At the grounding line, a no-displacement boundary condition is applied

$$\vec{U} = 0. \quad (10)$$

The boundary condition for  $\Phi$  at the sea bottom  $z = B_s(x, y)$ , is

$$\vec{n} \cdot \vec{\nabla} \Phi = 0, \quad (11)$$

where  $\vec{n}$  is the normal vector.

At the ice-shelf base,  $z=B(x, y)$ ,

$$\frac{\partial \Phi}{\partial z} = \frac{\partial w}{\partial t}, \quad (12)$$

where  $w$  is the vertical component of the ice-shelf displacement.

At the ice-shelf front,  $F(x, y)$ , an incident monochromatic wave with angular frequency  $\omega$  and amplitude  $A$  has the following potential:

$$\Phi(x, y, z) = \frac{Ag}{\omega} \sin(\vec{k} \cdot \vec{r}_2 + \omega t) \frac{\cosh k(z-B_s)}{\cosh kB_s}, \quad (13)$$

where  $\vec{r}_2 = \{x, y, 0\}$  and  $k$  is the wavenumber that satisfies the dispersion relationship

$$\omega^2 = kg \tanh kB_s. \quad (14)$$

### 3. Vertically Integrated Treatment of Wave-Induced Ice-Shelf Flexure

In order to gain insight in how flexural gravity waves propagate through the ice-shelf/subice-shelf cavity system, what their characteristics are (dispersion relation, wavelength, etc.), and how they relate to geometric properties of the ice shelf and its cavity, we consider a vertically integrated model of ice-shelf deformation and a vertically integrated model of potential flow (the shallow-water approximation) applied to a one-dimensional geometry (Figure 1). The ice-shelf deformation model is based on a thin-beam approximation [Timoshenko and Goodier, 1970], and described in detail by Sergienko [2005, 2013]. The major assumption of the thin-beam approximation is that the ice-shelf deformation can be described by a vertical displacement of a neutral plane  $\eta$ , which depends on the horizontal coordinate and is vertically uniform. Neglecting the acceleration term due to its smallness compared to other terms, a one-dimensional version of the vertically integrated form of (1) is

$$-\frac{\partial^2}{\partial x^2} \left( D \frac{\partial^2 \eta}{\partial x^2} \right) - \rho_w g \eta + p_w = 0, \quad (15)$$

where  $D = \frac{EH_i^3}{12(1-\nu^2)}$  is the ice-shelf flexural rigidity and  $p_w$  is wave-induced pressure defined by (8). Characteristic magnitudes of the flexural rigidity  $D$  are  $10^{14}$ – $10^{16}$  Pa m<sup>3</sup>. The acceleration term,  $\rho H_i \frac{\partial^2 \eta}{\partial t^2}$ , is on the order of 0.1 for the periods of flexural gravity oscillations considered here ( $\sim 0.003$  s<sup>−1</sup>). The corresponding deformational term,  $\frac{\partial^2}{\partial x^2} \left( D \frac{\partial^2 \eta}{\partial x^2} \right)$ , is on the order of 150, hence the assumption that the acceleration term can be neglected is well-justified.

The boundary conditions are no displacement at the grounding line ( $x=0$ ) and a prescribed bending moment  $M = -D \frac{\partial^2 \eta}{\partial x^2}$  at the ice-shelf front ( $x=L$ ), i.e.,

$$\eta|_{x=0} = 0 \quad (16a)$$

$$M|_{x=L} = \rho_w g H_i^3 \left( \frac{\rho^3}{6\rho_w^3} - \frac{\rho^2}{4\rho_w^2} \right). \quad (16b)$$

The subice-shelf wave propagation is described by the shallow-water theory [e.g., Stoker, 1957]

$$\frac{\partial \eta}{\partial t} = -\frac{\partial}{\partial x} \left( H \frac{\partial \Phi}{\partial x} \right), \quad (17)$$

where  $H$  is the water-column depth in the ice-shelf cavity. This simplification is justified by the fact that short surface waves are predominantly reflected from the ice-shelf front

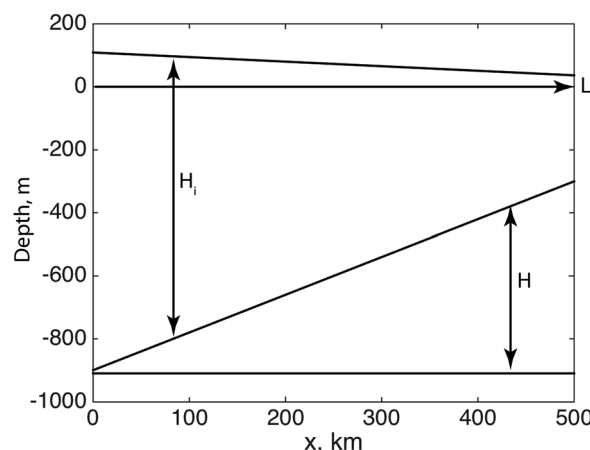


Figure 1. Geometry of a one-dimensional system.



and cannot propagate into the cavity, and is supported by observations [MacAyeal *et al.*, 2006; Bromirski *et al.*, 2010].

The boundary conditions are no flow at the grounding line ( $x = 0$ ) and a prescribed velocity potential at the ice front ( $x = L$ )

$$\left. \frac{\partial \Phi}{\partial x} \right|_{x=0} = 0 \quad (18a)$$

$$\Phi|_{x=L} = \Phi_0. \quad (18b)$$

It is possible to reduce two equations (15) and (17) to one equation for  $\Phi$  only by differentiating (15) with respect to time and taking into account (17)

$$\frac{\partial^2}{\partial x^2} \left[ D \frac{\partial^3}{\partial x^3} \left( H \frac{\partial \Phi}{\partial x} \right) \right] + \rho_w g \frac{\partial}{\partial x} \left( H \frac{\partial \Phi}{\partial x} \right) - \rho_w \frac{\partial^2 \Phi}{\partial t^2} = 0. \quad (19)$$

However, if the ice-shelf thickness varies slowly (circumstances considered here), spatial variations in flexural rigidity are substantially smaller compared with the variations of the water-column depth in this cavity. Therefore, the above equation could be written as

$$D \frac{\partial^5}{\partial x^5} \left( H \frac{\partial \Phi}{\partial x} \right) + \rho_w g \frac{\partial}{\partial x} \left( H \frac{\partial \Phi}{\partial x} \right) - \rho_w \frac{\partial^2 \Phi}{\partial t^2} = 0. \quad (20)$$

This equation, together with the boundary conditions (18) describe propagation of the flexural gravity waves in the ice-shelf/subice-shelf cavity excited by incident waves  $\Phi_0$  at the ice-shelf front. The considered problem is linear; therefore, the ice-shelf flexure caused by the spectrum of incident ocean waves is a linear superposition of the ice-shelf flexure excited by monochromatic waves comprising the wave spectrum.

### 3.1. Approximate Analytic Solutions

In order to investigate the effects of a monochromatic incident wave, the velocity potential at the ice front  $\Phi_0$  is chosen in a form  $\Phi_0(t) = Ae^{i\omega t}$ , where  $A$  is the amplitude, assumed to be constant, and  $\omega$  is the incident wave frequency. Similar to studies of propagation of shallow water waves through water with slowly varying depth [e.g., *Didenkulova et al.*, 2009] are assumed here that the velocity potential,  $\Phi$ , and the ice-shelf vertical displacement,  $\eta$ , have the following forms:

$$\Phi = \phi(x) e^{i[\Psi(x) + \omega t]} \quad (21a)$$

$$\eta = \xi(x) e^{i[\Psi(x) + \omega t]}, \quad (21b)$$

where  $\phi(x)$ ,  $\xi(x)$  and  $\Psi(x)$  are the real functions of location only (the local amplitudes of the velocity potential and the ice-shelf deflection, and the phase, respectively). Substitution of  $\Phi$  in the form (21a) into (20) yields two equations—one for the real part and the other for the imaginary part:

$$[DHk^6 + \rho_w g k^2 H - \rho_w \omega^2] \phi - D \left\{ \frac{d^5 H}{dx^5} \frac{d\phi}{dx} + 4 \frac{d^4 H}{dx^4} \left( \frac{d^2 \phi}{dx^2} - k^2 \phi \right) + 10 \frac{d^3 H}{dx^3} \left( \frac{d^3 \phi}{dx^3} - 3k^2 \phi \right) + \dots \right. \\ \left. 10 \frac{d^2 H}{dx^2} \left( \frac{d^4 \phi}{dx^4} - 6k^2 \frac{d^2 \phi}{dx^2} + k^4 \phi \right) + 5 \frac{dH}{dx} \left( \frac{d^5 \phi}{dx^5} - 10k^2 \frac{d^3 \phi}{dx^3} + 5k^4 \frac{d\phi}{dx} \right) + \dots \right. \quad (22a)$$

$$\left. H \left( \frac{d^6 \phi}{dx^6} - 15k^2 \frac{d^4 \phi}{dx^4} + 15k^4 \frac{d^2 \phi}{dx^2} \right) \right\} + \rho_w g \left\{ \frac{dH}{dx} \frac{d\phi}{dx} + H \frac{d^2 \phi}{dx^2} \right\} = 0$$

$$D \left\{ \frac{d^5 H}{dx^5} \phi + 8 \frac{d^4 H}{dx^4} \frac{d\phi}{dx} + 10 \frac{d^3 H}{dx^3} \left( 3 \frac{d^2 \phi}{dx^2} - k^2 \phi \right) + 10 \frac{d^2 H}{dx^2} \left( 4 \frac{d^3 \phi}{dx^3} - 4k^2 \frac{d\phi}{dx} \right) + \dots \right. \\ \left. 5 \frac{dH}{dx} \left( 5 \frac{d^4 \phi}{dx^4} - 10k^2 \frac{d^2 \phi}{dx^2} + k^4 \phi \right) + H \left( 6 \frac{d^5 \phi}{dx^5} - 20k^2 \frac{d^3 \phi}{dx^3} + 6k^4 \frac{d\phi}{dx} \right) \right\} + \dots \quad (22b)$$

$$\rho_w g \left\{ \frac{dH}{dx} \phi + 2H \frac{d\phi}{dx} \right\} = 0,$$

where  $k = \frac{d\psi}{dx}$  is the wavenumber. The first of these expressions, equation (22a), is the generalized dispersion relationship. For slowly varying depth  $H$ , the first term of equation (22a) is much larger than the other terms. Hence, the dispersion relationship can be written as

$$DHk^6 + \rho_w g k^2 H \simeq \rho_w \omega^2. \quad (23)$$

The real root of this equation is

$$k = \left[ \left( \frac{\rho_w \omega^2}{2DH} + \sqrt{\left( \frac{\rho_w \omega^2}{2DH} \right)^2 + \left( \frac{\rho_w g}{3D} \right)^3} \right)^{1/3} + \left( \frac{\rho_w \omega^2}{2DH} - \sqrt{\left( \frac{\rho_w \omega^2}{2DH} \right)^2 + \left( \frac{\rho_w g}{3D} \right)^3} \right)^{1/3} \right]^{1/2}. \quad (24)$$

Rearranging terms, this expression can be written as

$$k = (2k_f^4 k_{sw}^2)^{1/6} \left[ \left( 1 + \sqrt{1 + \alpha} \right)^{1/3} + \left( 1 - \sqrt{1 + \alpha} \right)^{1/3} \right]^{1/2}, \quad (25)$$

where  $k_f = \left( \frac{\rho_w g}{4D} \right)^{1/4}$  is the wave number of buoyancy-forced flexural bending of an ice shelf with flexural rigidity  $D$  [Sergienko, 2005];  $k_{sw} = \frac{\omega}{\sqrt{gH}}$  is the wave number of a shallow water wave propagating in the open ocean with the same water depth as the ice-shelf cavity water-column thickness; and  $\alpha$  is a dimensionless parameter

$$\alpha \equiv \frac{4}{27} \frac{\rho_w g^3 H^2}{D \omega^4} = \frac{16}{27} \left( \frac{k_f}{k_{sw}} \right)^4. \quad (26)$$

The group and phase velocities  $V_g = \frac{\partial \omega}{\partial k}$ ,  $V_p = \frac{\omega}{k}$ , respectively, are

$$V_g = V_{sw} \frac{\frac{3}{4} \left( \frac{k}{k_f} \right)^4 + 1}{\sqrt{\frac{1}{4} \left( \frac{k}{k_f} \right)^4 + 1}} \quad (27a)$$

$$V_p = V_{sw} \sqrt{\frac{1}{4} \left( \frac{k}{k_f} \right)^4 + 1}, \quad (27b)$$

where  $V_{sw} = \sqrt{gH}$  is the group and phase velocity of shallow water waves. The flexural gravity waves are dispersive, in contrast to nondispersive shallow water waves.

It is possible to make further simplifications of the dispersion relationship, equation (24), if  $\alpha \ll 1$  or  $\alpha \gg 1$ . The former case corresponds to high frequency incident waves, and the latter case corresponds to low frequency waves. In both cases, the shallow-water approximation should still be satisfied, and the length of an incident wave is assumed to be much longer than the water-column depth,  $H$ .

For geometries of ice shelves and their cavities such that  $\alpha \ll 1$ ,

$$k \simeq \left( \frac{\rho_w \omega^2}{DH} \right)^{1/6} = (2k_{sw})^{1/3} k_f^{2/3}. \quad (28)$$

It should be noted that in contrast to the open ocean shallow water waves, these waves are dispersive; their group,  $V_g$ , and phase,  $V_p$ , velocities are

$$V_g = 3V_p = 3k^2 \sqrt{H \frac{D}{\rho_w}}. \quad (29)$$

Analysis of the above expressions shows that the short flexural gravity waves propagate faster than long waves ( $k \ll 1$ ), and they travel faster through ice shelves with deeper cavities and stiffer ice shelves (having larger  $D$ ).

In the case of  $\alpha \gg 1$  ( $k_{sw} \ll k_f$ , low-frequency incident waves)

$$k \simeq k_{sw}. \quad (30)$$

The corresponding group and phase velocities are the same as the shallow-water case:

$$V_g = V_p = V_{sw} = \sqrt{gH}. \quad (31)$$

In this case, the flexural gravity waves are nondispersive, and their propagation is not affected by the presence of the ice shelf.

The amplitude of the velocity potential,  $\phi(x)$ , is determined from equation (22b). Using the same assumption that all functions of  $x$  vary slowly, the lowest order expression is

$$D \left( 5k^4 \phi \frac{dH}{dx} + 6k^4 H \frac{d\phi}{dx} \right) + \rho_w g \left( \frac{dH}{dx} \phi + 2H \frac{d\phi}{dx} \right) \simeq 0. \quad (32)$$

A solution of this equation with a boundary condition (18) is

$$\phi(x) = A \exp \left( \int_L^x dx' \frac{H'(x')}{H(x')} \frac{5k(x')^4 D(x') + \rho_w g}{6k(x')^4 D(x') + 2\rho_w g} \right), \quad (33)$$

where  $H' = \frac{dH}{dx}$ . Substitution of  $\Phi$  and  $\eta$  in a form of (21a) and (21b) into expression (17) yields the following expression for the real part:

$$\omega \xi = H \left( k^2 \phi - \frac{d^2 \phi}{dx^2} \right) - \frac{dH}{dx} \frac{d\phi}{dx}. \quad (34)$$

With  $H(x)$  and  $\phi(x)$  varying slowly with  $x$ , the balance of the largest terms of this expression yields

$$\xi(x) \simeq \frac{k^2}{\omega} H \phi, \quad (35)$$

where  $\phi(x)$  is determined by (33).

The maximum magnitude of stress associated with the ice-shelf flexure,  $\sigma_f$ , is achieved at the top and bottom surfaces of the ice shelf, and is determined by the curvature of the ice-shelf flexure [Timoshenko and Goodier, 1970]

$$|\sigma_f| = \frac{EH_i}{1-\nu^2} \left| \frac{d^2 \eta}{dx^2} \right|. \quad (36)$$

Under the same assumption of slow varying functions of  $x$

$$|\sigma_f| \simeq \frac{EH_i}{1-\nu^2} \frac{k^4}{\omega} H \phi. \quad (37)$$

For the two limiting cases of  $\alpha \ll 1$  (dispersive flexural gravity waves) and  $\alpha \gg 1$  (nondispersive flexural gravity waves), where  $\alpha$  is defined by (26), the expressions for  $\xi$  and  $\sigma_f$  can be obtained by substituting simplified expressions for  $k$ , equations (28) and (30). If  $\alpha \ll 1$ , the expression for  $\phi$ , equation (33), becomes

$$\phi(x) \simeq A \left( \frac{H_L}{H(x)} \right)^{5/6}, \quad (38)$$

where  $H_L$  is the subice-shelf cavity water-column thickness at the ice-shelf front. The expression for the amplitude of the ice-shelf vertical deflection,  $\xi$ , becomes

$$\xi(x) \simeq A \left[ \frac{12(1-\nu^2)\rho_w}{E\omega} \right]^{1/3} \frac{H_i H_L^{1/3}}{H^{1/6}}, \quad (39)$$

and the maximum wave-induced flexural stress,  $\sigma_f$ , is

$$|\sigma_f| \simeq A(12\rho_w)^{2/3} \left( \frac{E\omega}{1-\nu^2} \right)^{1/3} \frac{H_L^{5/6}}{H_i(x)H(x)^{1/2}}. \quad (40)$$

In circumstances, where  $\alpha \gg 1$  and  $k$  is described by equation (30), the simplified expression for  $\phi$  is

$$\phi(x) \simeq A \left( \frac{H_L}{H(x)} \right)^{1/2}, \quad (41)$$

the expression for  $\zeta$  is

$$\zeta(x) \simeq A \frac{\omega}{g} \left( \frac{H_L}{H} \right)^{1/2}, \quad (42)$$

and the expression for  $\sigma_f$  is

$$|\sigma_f| \simeq A \frac{EH_L \omega^3}{g^2(1-\nu^2)} \left[ \frac{H_L}{H(x)^3} \right]^{1/2}. \quad (43)$$

### 3.2. Comparison of Simplified Analytic Expressions With Numerical Solutions

In order to assess the validity and accuracy of the approximate expressions for the limiting cases of  $\alpha \ll 1$  and  $\alpha \gg 1$  derived above, they are compared with numerical solutions of the vertically integrated model of flexural gravity waves of a one-dimensional ice-shelf/subice-shelf cavity system described by equations (15) and (17) and boundary conditions (16) and (18). The simulations are performed for an idealized geometry (Figure 1) such that the ice-shelf thickness and the subice-shelf depth are linear functions of the coordinate  $x$ . Figures 2 and 3 show results for the case  $\alpha \ll 1$  (the incident wave period is 100 s) and  $\alpha \gg 1$  (the incident wave period is 600 s), respectively. In both cases, the approximate expressions are in closer agreement with the numerical results where the respective conditions on  $\alpha$  are satisfied. In the case of high frequency incident waves (100 s),  $\alpha \simeq 10^{-1}$  near the ice-shelf front, and the discrepancy between the numerical solution and approximate expression for the flexural stress is large,  $\sim 60\%$  (Figure 2d). As  $\alpha$  decreases toward the grounding line, the discrepancy diminishes, and is within 5% in the vicinity of the grounding line. In the

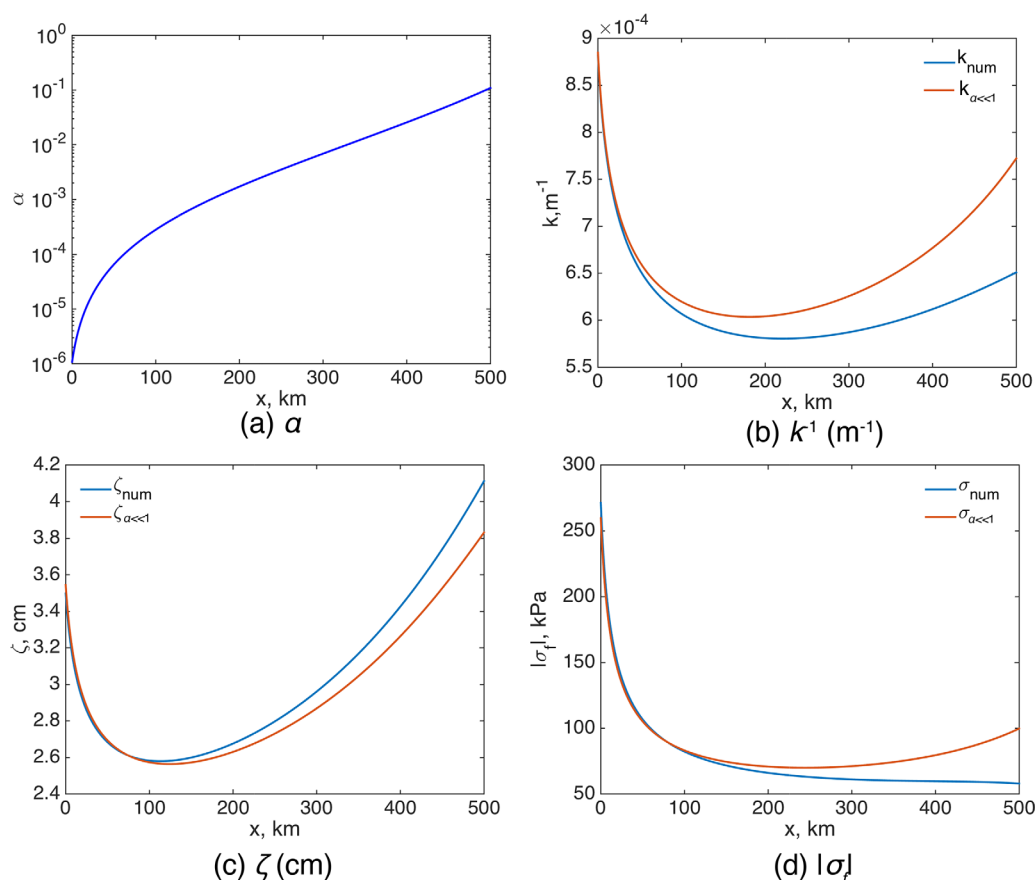


**Figure 2.** The effects of high-frequency flexural gravity waves ( $\alpha \ll 1$ ). (a) Parameter  $\alpha$ , defined by equation (26); (b) wave number,  $k$ , blue line—exact values equation (25), red line—approximate solution, equation (28); (c) amplitude of the ice-shelf vertical displacement,  $\zeta(x)$ , blue line—numerical solution, red line—approximate expression, equation (39); (d) the magnitude of the ice-shelf flexural stress,  $|\sigma_f|$ , blue line—numerical solution, red line—approximate expression, equation (40).

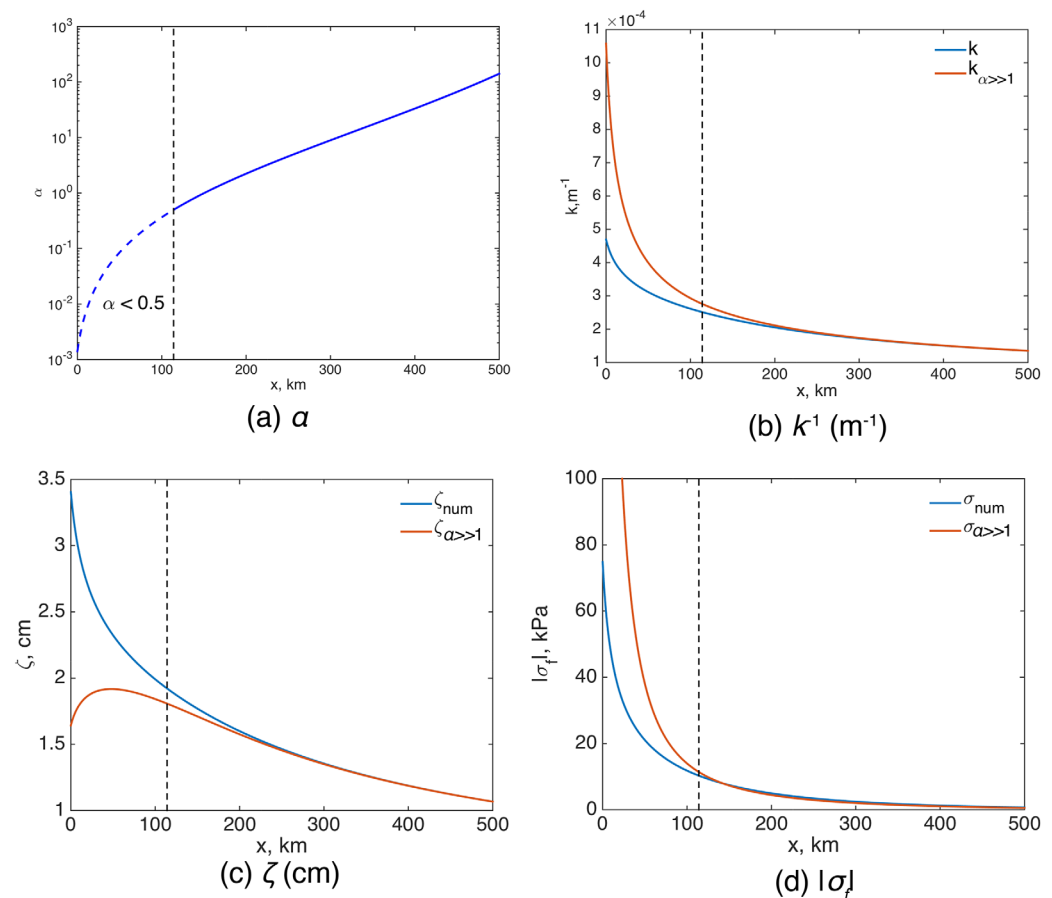


**Figure 3.** The effects of low-frequency flexural gravity waves. (a) Parameter  $\alpha$ , defined by equation (26); (b) wave number,  $k$ , blue line—exact values equation (25), red line—approximate solution, equation (30); (c) amplitude of the ice-shelf vertical displacement,  $\zeta(x)$ , blue line—numerical solution, red line—approximate expression, equation (42); (d) the magnitude of the ice-shelf flexural stress,  $|\sigma_f|$ , blue line—numerical solution, red line—approximate expression, equation (43). Vertical dashed line denotes a location of  $\alpha = 0.5$ .

case of low frequency incident waves (600 s), the agreement between numerical solutions and the approximate expressions is better near the ice front where  $\alpha \simeq 10^2$ . The agreement deteriorates toward the grounding line as  $\alpha$  decreases and the approximation  $\alpha \gg 1$  fails (Figure 3, the vertical dashed line shows the location where  $\alpha = 0.5$ ).

A typical ice shelf configuration is such that it is thinner near the ice front and progressively thickens toward the grounding line; the water-column depth is larger near the ice front and shallows toward the grounding line. Hence, a typical distribution of the parameter  $\alpha$  is such that it is relatively large near the ice front and decreases toward the grounding line. This suggests that the expressions for  $\alpha \gg 1$  can be used near the ice front and  $\alpha \ll 1$  in the vicinity of the grounding line. Figure 4 shows results of numerical simulations and approximate expressions for the case of flexural gravity wave with 300 s period. For the considered geometry (Figure 1), the parameter  $\alpha$  varies from  $\sim 10$  at the ice front to  $\sim 10^{-4}$  near the grounding line. The derived approximate expressions for  $\alpha \gg 1$  and  $\alpha \ll 1$  provide a good approximation of the ice-shelf vertical displacement and the flexural stresses near the ice front (equation (43)) and the grounding line (equation (40)), respectively.

### 3.3. Analysis of the Behavior of High-Frequency Flexural and Low-Frequency Flexural Gravity Waves

A good agreement between the numerical solutions and simplified analytic expressions suggests that the latter can be used to gain insights into the behavior of the flexural gravity waves propagating through the ice-shelf/subice-shelf cavity system. The approximate expressions for the amplitude of the ice-shelf vertical deflection, equations (39) and (42), suggest different behavior in response to incident ocean waves with different frequencies. In the case of  $\alpha \gg 1$  (or  $k_{sw} \ll k_f$ ), there is no dependence on characteristics of the ice shelf; and the vertical displacement is determined by the subice-shelf water-column thickness and the

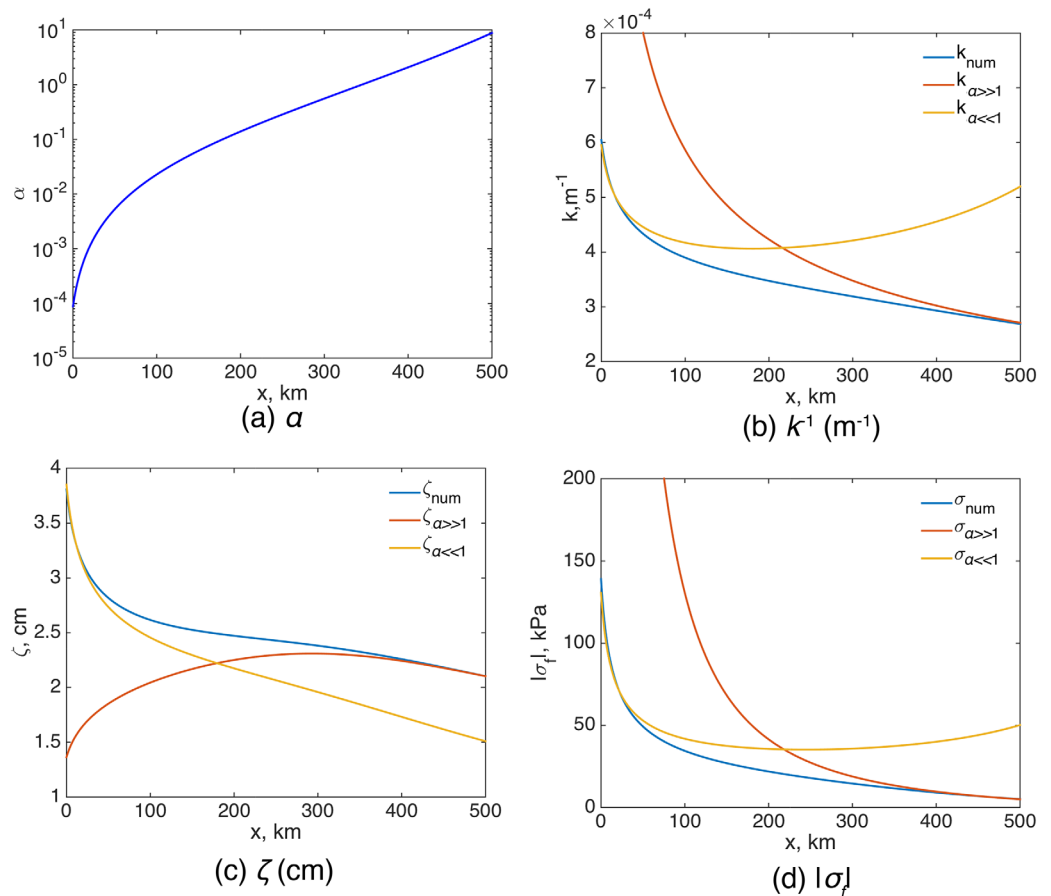


**Figure 4.** The effects of medium-frequency flexural gravity waves ( $\alpha \gg 1$ ). (a) Parameter  $\alpha$ , defined by equation (26); (b) wave number,  $k$ , blue line—exact values equation (25), red line—approximate expression for the  $\alpha \gg 1$  case, equation (30), yellow line—approximate expression for the  $\alpha \ll 1$  case, equation (28); (c) amplitude of the ice-shelf vertical displacement,  $\zeta(x)$ , blue line—numerical solution, red line—approximate expression for the  $\alpha \gg 1$  case, equation (42), yellow line—approximate expression for the  $\alpha \ll 1$  case, equation (39); (d) the magnitude of the ice-shelf flexural stress,  $|\sigma_f|$ , blue line—numerical solution, red line—approximate expression the  $\alpha \gg 1$  case, equation (43), yellow line—approximate expression for the  $\alpha \ll 1$  case.

frequency of the incident wave. This suggests that the flexural gravity waves excited by low-frequency ocean waves propagate in a fashion similar to shallow water waves. In contrast, in the case of  $\alpha \ll 1$ , the amplitude of the ice-shelf vertical deflection depends linearly on the ice-shelf thickness and exponentially on Young's modulus. In this case, the dependence on the water-column depth is weaker than in the case of  $\alpha \gg 1$  (an exponent  $-1/6$  versus  $-1/2$ ). These different dependencies on the ice-shelf and subice-shelf cavity characteristics result in different spatial distributions of the amplitude of the ice-shelf deflection. In the case of higher frequency waves ( $\alpha \ll 1$ ) the amplitude decreases, and in the case lower frequency waves ( $\alpha \gg 1$ ) it increases away from the ice-shelf front. Such a behavior is determined by the spatial distribution of the ice-shelf thickness and the water-column depth.

Analysis of the expressions for  $\sigma_f$ , equations (40) and (43), shows that incident shallow-water waves with higher frequencies ( $\alpha \ll 1$ ) exciting dispersive flexural gravity waves in the ice-shelf/subice-shelf cavity system result in larger flexural stresses compared to the stresses excited by waves with lower frequency ( $\alpha \gg 1$ ) (Figures 2d and 3d). The inverse dependence of the flexural stress on the water-column thickness suggests that ice shelves with shallower water depth cavities have larger flexural stresses. These stresses have also higher magnitudes if the ice shelves are relatively thin.

#### 4. Flexural Gravity Waves on the Ross Ice Shelf

The results of a simplified one-dimensional treatment of ocean waves interactions with an ice-shelf/subice-shelf-cavity system presented above give an idea about the general behavior of the system—the dispersion



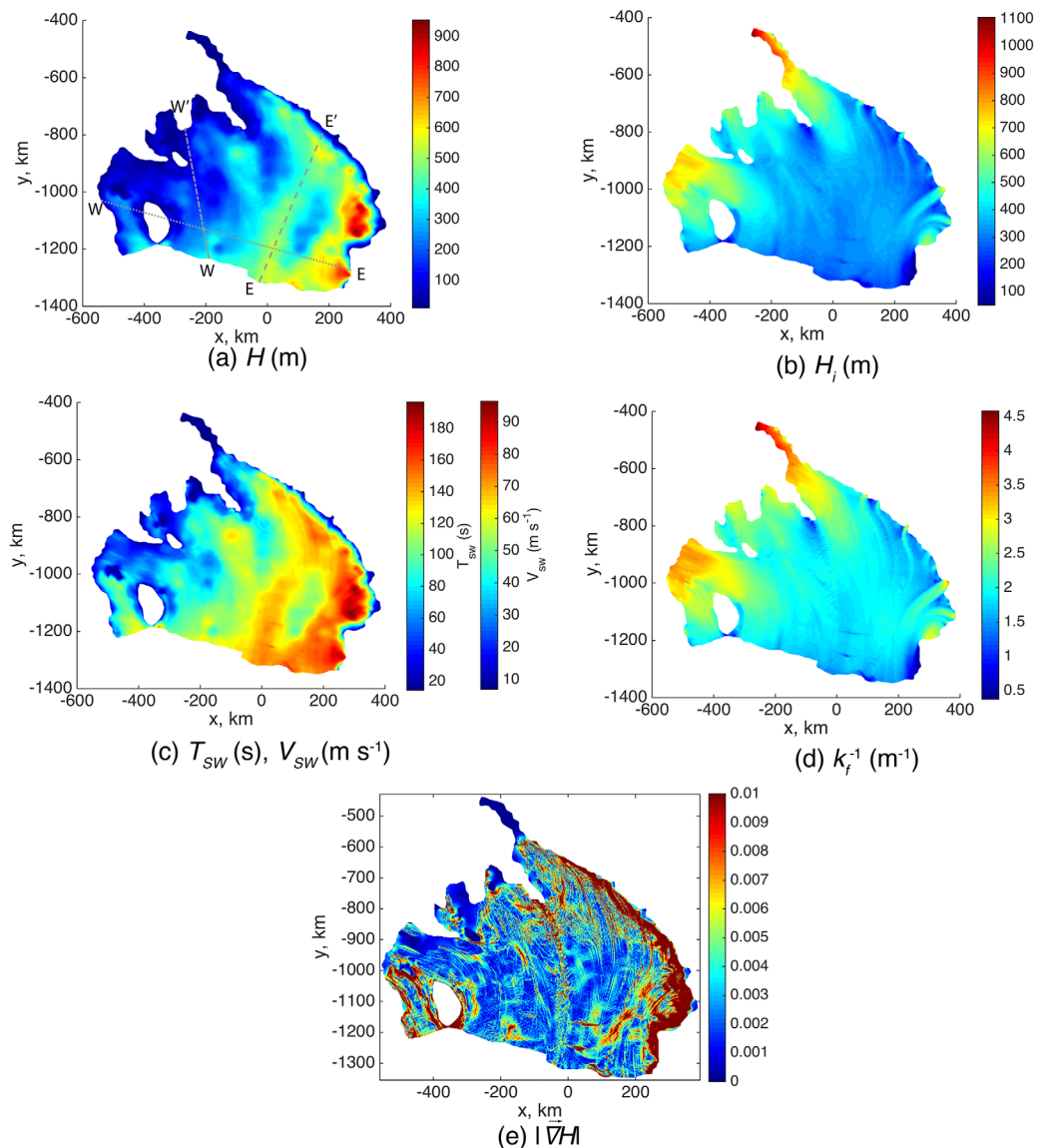


**Figure 5.** Geometry of the RIS cavity; (a) the cavity water-column depth (m); (b) the ice-shelf thickness (m); (c) minimal period of an incident ocean wave (s) that satisfies shallow water approximation ( $\lambda > 20 H$ ) and shallow water wave velocity  $V_{sw}$  ( $\text{m s}^{-1}$ ); (d) wavelength of buoyancy-forced ice-shelf flexure  $k_f^{-1}$  (km); and (e) the gradient of the cavity water-column thickness.

relationship of the flexural gravity waves, the spatial variability of the magnitudes of the flexural stresses, their dependence on the geometric parameters of the system (e.g., the water-column and ice-shelf thicknesses), the incident wave frequency, etc. However, apart from ice tongues, which geometries can be considered similar to a configuration considered in the previous section, the majority of the ice shelves and their cavities cannot be approximated by one-dimensional geometry and a simplified treatment. The Ross Ice Shelf and its cavity are considered as an example of a realistic geometry. The Bedmap 2 data set [Fretwell *et al.*, 2013] provides the RIS ice thickness and bathymetry of its cavity with a 1 km spatial resolution. Both, the water-column and the ice-shelf thickness are highly spatially variable (Figures 5a and 5b). The north-south differences in the RIS ice thickness (Figure 5b) manifest themselves in flexure, e.g., the characteristic length of the buoyancy-forced bending ( $k_f^{-1}$  shown in Figure 5d). The wavelength progressively increases from the RIS front, where it is  $\sim 2$  km, toward the grounding line, where it is  $\sim 3$ – $4$  km. The RIS cavity has a complex geometry. Its western part has a substantially deeper water column and an overall thinner ice shelf than the eastern part of the cavity. The ice shelf thickness increases from 200–350 m at the ice-shelf front to

400–900 m at the grounding line. The prominent east-west differences in the RIS cavity configuration have strong effects on how flexural gravity waves should be treated, e.g., Figure 5 shows minimal period of an incident ocean wave that satisfies the shallow water approximation (the wavelength  $\lambda > 20H$ ), and how shallow water waves would propagate through the open water with the same depth as the RIS water-column depth. In the RIS case, the shallow water approximation is valid for very long-period incident waves ( $\geq 200$  s).

In order to account for the effects of the horizontal spatial variability of the ice-shelf/subice-shelf cavity system, and also investigate the vertical distribution of the ice-shelf flexural stresses, a three-dimensional coupled model of the ice-shelf elastic deformation and the wave propagation in the subice-shelf cavity described by equations (1), (2), (5) and boundary conditions (6)–(13) are solved numerically using a finite-element solver package COMSOL<sup>TM</sup>.

The numerical simulations are performed for monochromatic infragravity-wave forcing in a manner to explore different frequencies and angles of incidence at the RIS front. The choice of wave frequencies is motivated by field observations on the RIS [Bromirski *et al.*, 2015]. A network of broadband seismometers has recorded the arrival and propagation of infragravity ocean waves (75–400 s) in the interior of the RIS and its cavity at least 100 km from the ice front. In these simulations, the potential flow in the RIS cavity is described by a three-dimensional velocity potential  $\Phi$ , equation (5) to avoid violation of the shallow water approximation.

As mentioned above, due to linearity of the considered model, the net effect of the spectrum of ocean waves can be treated as a linear superposition of the effects of monochromatic waves. In contrast to the geometric configuration with one horizontal dimension that allows open ocean waves to impact the ice-shelf front in the normal direction only, in geometries with two horizontal dimensions ocean waves can

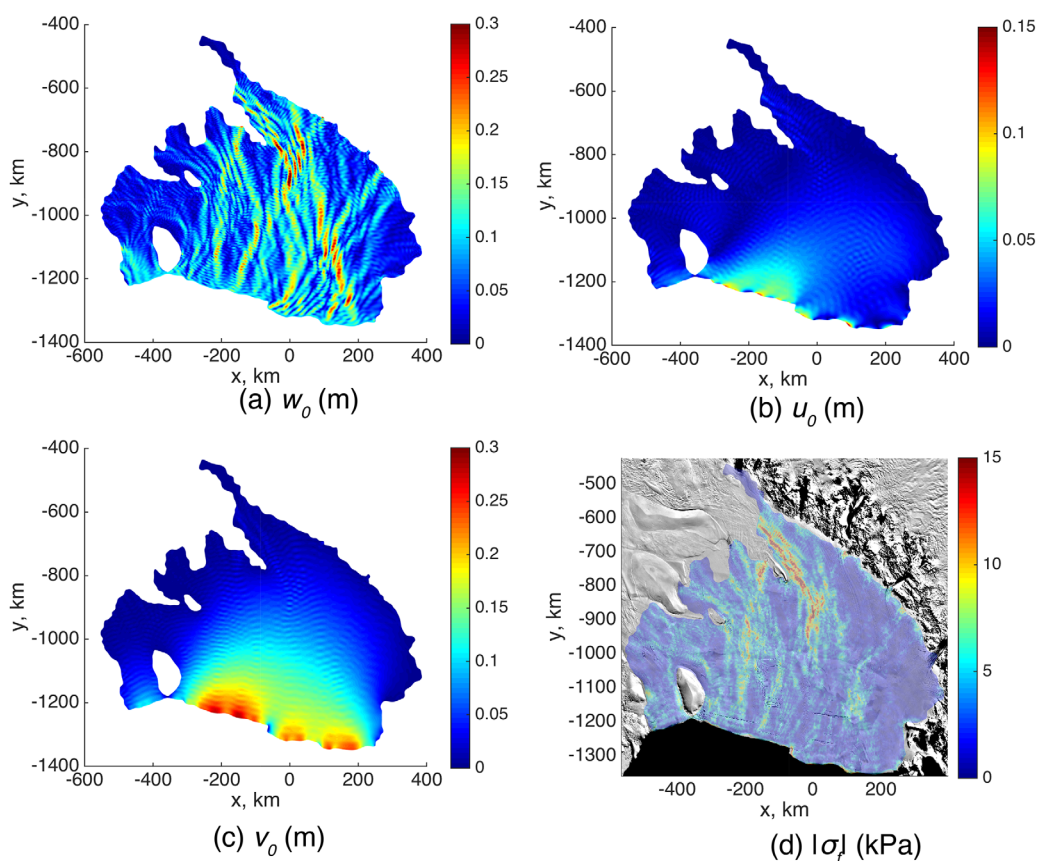


**Figure 6.** The effects of a 300 s wave incident normally to the ice front. (a) Amplitude of the RIS surface vertical displacement (m); (b) amplitude of the RIS surface E-W horizontal displacement (m); (c) amplitude of the RIS surface S-N horizontal displacement (m); and (d) amplitude of the effective stress at the ice-shelf surface (kPa), background MODIS image of the Ross Ice Shelf [Haran *et al.*, 2005].

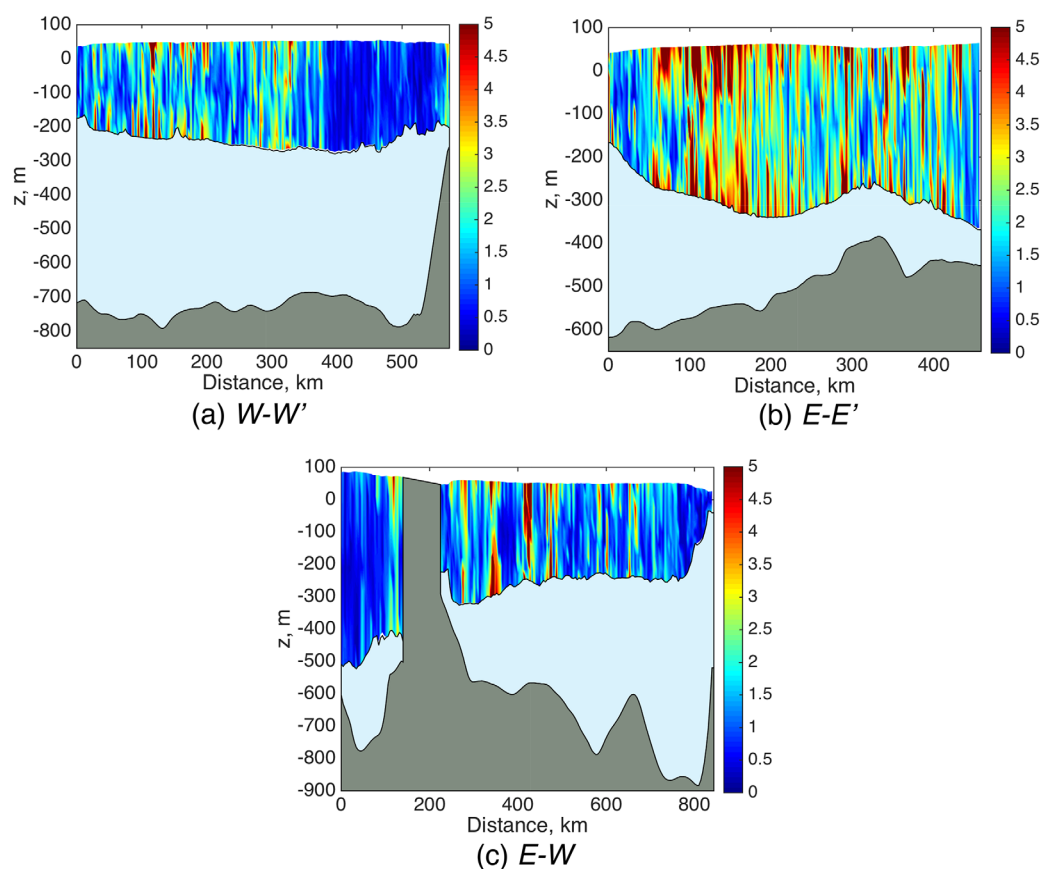


**Figure 7.** Vertical distributions of the magnitude of the effective stress (kPa) induced by a 300 s wave incident normally to the ice front. (a) W-W' cross section, (b) E-E' cross section, and (c) E-W cross section. The locations of the cross sections are shown in Figure 5.

reach the ice-shelf front at various angles. Two model runs are performed to simulate flexural gravity waves in the RIS/subice-shelf cavity system excited by ocean waves incident normal and parallel to the RIS front. Both waves have the same period 300 s and amplitude 10 cm.

Results of simulations for the normal incident wave are summarized in Figures 6–8. The amplitudes of the ice-shelf surface displacements are strongly spatially heterogeneous. The vertical displacements exhibit spatial organizations such that relatively large amplitudes (10–20 cm) are observed as narrow ( $\sim 20$  km), beam-like formations with smaller amplitudes (1–3 cm) outside them. These high-amplitude beams are oriented predominantly in the north-south direction. The RIS horizontal displacements (Figures 6b and 6c) are more homogeneous and their magnitudes decay away from the ice-front. Outside of the beams characterized by large vertical displacements, the horizontal displacements are substantially larger (5–10-fold) than the horizontal ones in  $\sim 200$ – $300$  km zone from the ice front. The effective stress at the RIS surface caused by such deformation also exhibits a beam-like spatial organization (Figure 6d). The largest magnitudes ( $\sim 15$  kPa) are achieved near Cray Ice Rise [MacAyeal *et al.*, 1987], where the gradients of the cavity water-column depth are large (Figure 5e). The vertical distribution of the effective stress is highly heterogeneous as well. Figure 7 shows the effective stress distribution along three cross sections shown in Figure 5a. The ice shelf experiences flexural stresses through its whole depth. The largest magnitudes are achieved at the ice-shelf top and bottom surfaces. Depending on the location, some parts of the RIS do not experience any flexural stresses.

The beam-like organization of the vertical displacement strongly depends on the direction of the incident ocean wave propagation. Figure 8 summarizes results of simulations of the ocean wave propagating parallel to the ice front eastward (left column) and westward (right column). The vertical displacements have beam-like patterns oriented obliquely to the ice-shelf front (Figures 8a and 8b). The horizontal displacements

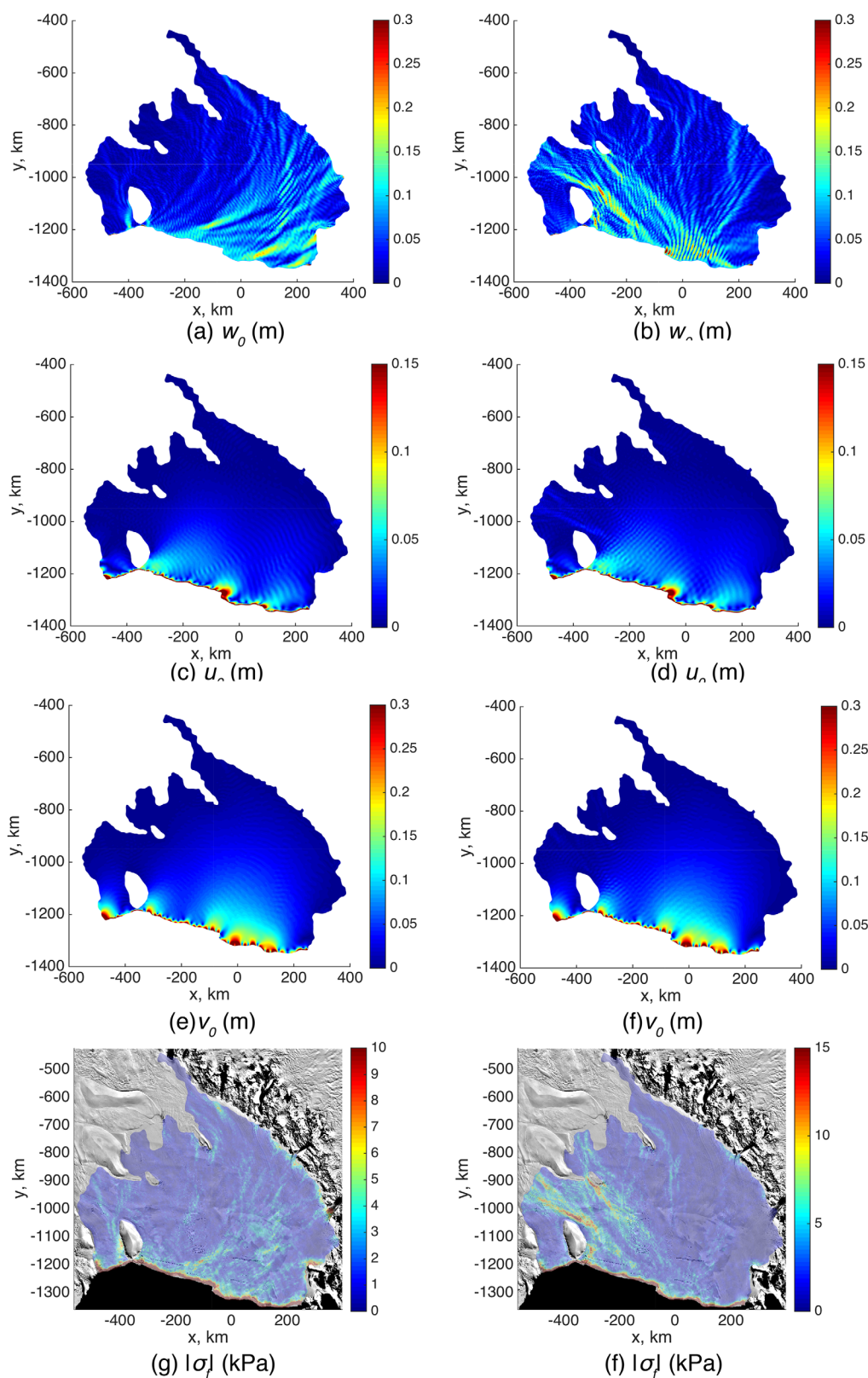


**Figure 8.** The effects of a 300 s wave propagating parallel to the RIS front: left column—eastward, left column—westward. Plots are the same as in Figure 6.



have less spatial variability. The largest magnitudes of the horizontal displacements are observed at the ice-shelf front that are about an order of magnitude larger than the vertical displacements, and decay quickly away from the ice front (Figures 8c–8f). The largest surface effective stresses are observed at the ice front (Figures 8g–8h). Away from the ice front, the effective stresses have beam-like spatial organization mimicking the spatial distributions of the vertical displacement.

To assess the effects of the incident wave periods, a simulation has been performed with a 100 s ocean wave incident normal to the RIS front. The vertical displacements have beam-like spatial structure as well (Figure 9a). However, the beams are narrower ( $\sim 7$ – $10$  km) compared to those obtained in simulations with 300 s incident wave (Figure 6a), they are more numerous and have more complex organization with some oriented obliquely to the ice front. In contrast to the simulations of the 300 s incident wave, the largest magnitudes of the vertical displacements are observed at the RIS front, and they are smaller toward the grounding line. The horizontal displacements have similar spatial patterns in simulations of 100 and 300 s incident waves. They have large magnitudes at the ice front that decay away from it (Figures 9b and 9c). The surface effective stress has a beam-like spatial pattern that resembles the pattern of the vertical displacements (Figure 9d). The magnitudes of the surface effective stresses are larger ( $\sim 50\%$ ) in simulations of 100 s incident wave compared to those in simulations with 300 s incident wave (Figure 6d). This is due to larger spatial variability of the vertical displacement, and a consequence larger vertical strains. The vertical distribution of the effective stress (Figure 10) has large spatial variability and also large magnitudes compared to those obtained in 300 s incident wave simulations (Figure 7). This is again due to larger strains associated with higher spatial variability of the vertical displacements.

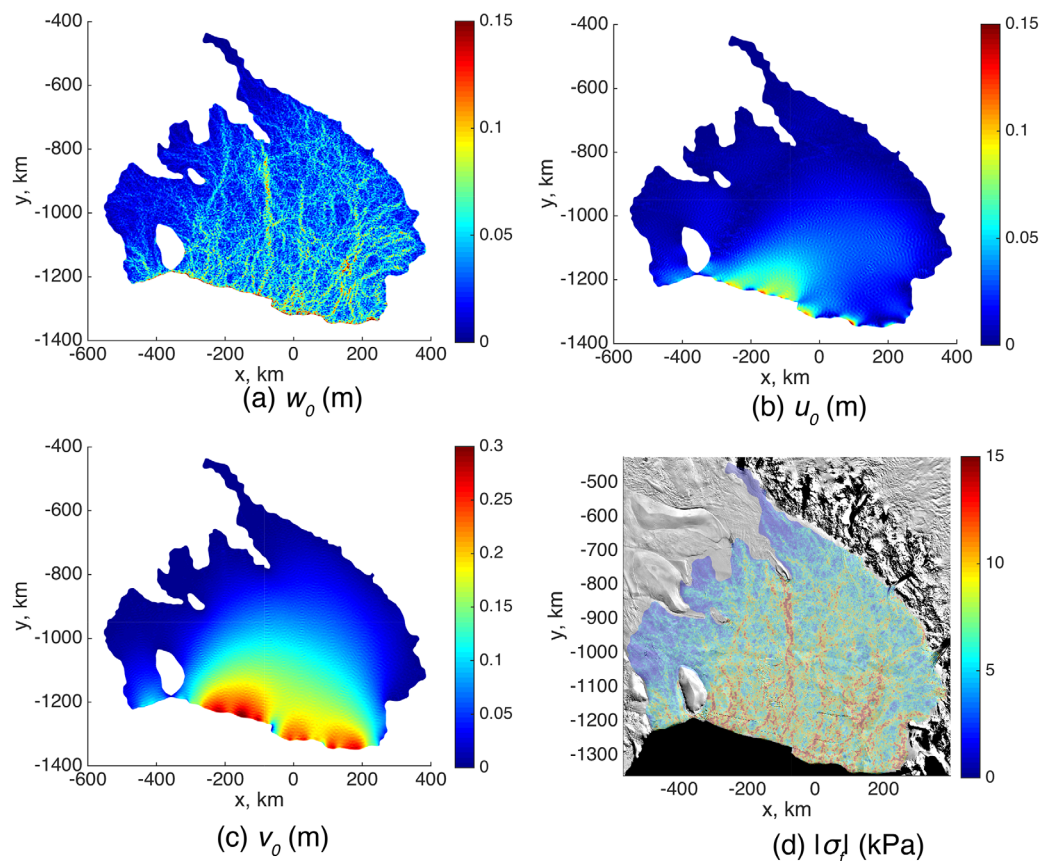


**Figure 9.** The effects of a 100 s wave incident normally to the ice front. (a) Amplitude of the RIS surface vertical displacement (m); (b) amplitude of the RIS surface E-W horizontal displacement (m); (c) amplitude of the RIS surface S-N horizontal displacement (m); and (d) amplitude of the effective stress at the ice-shelf surface (kPa), background MODIS image of the Ross Ice Shelf [Haran *et al.*, 2005].

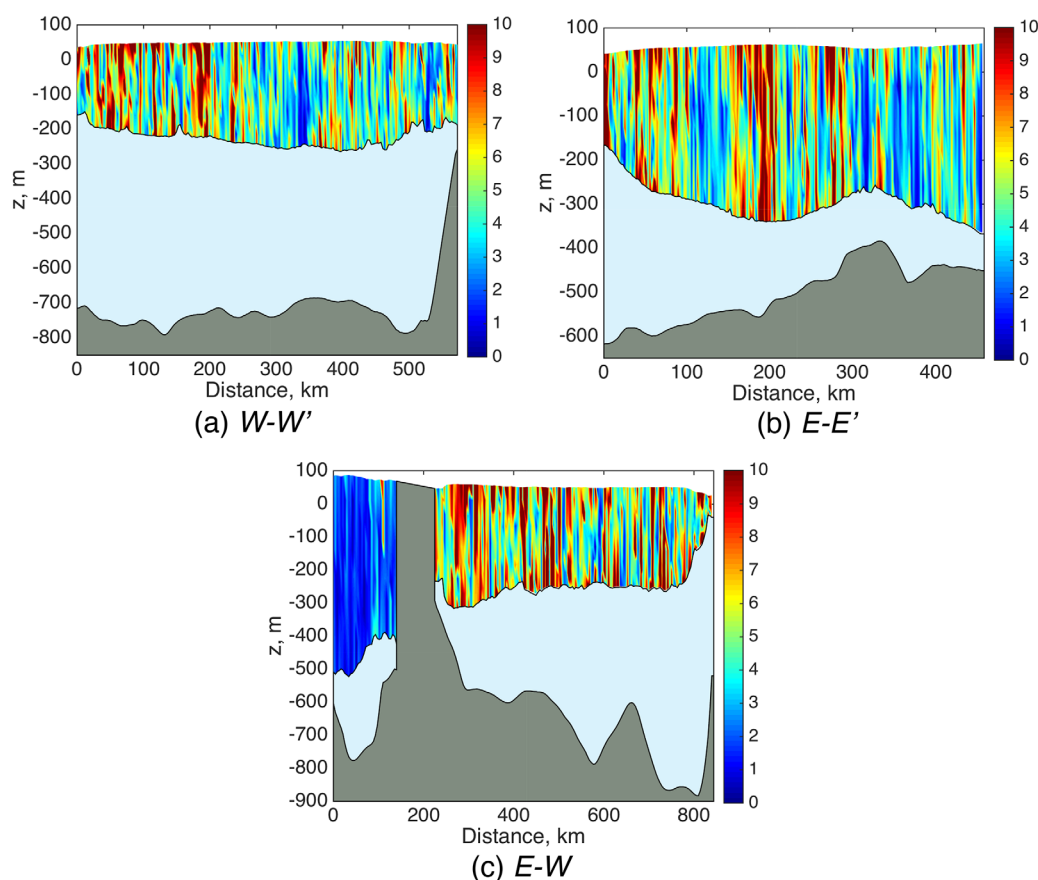


**Figure 10.** Vertical distributions of the magnitude of the effective stress (kPa) induced by a 100 s wave incident normally to the ice front. (a) W-W' cross section, (b) E-E' cross section, and (c) E-W cross section. The locations of the cross sections are shown in Figure 5.

## 5. Discussion and Conclusions

The major focus of the presented study is the effects of spatially variable geometric parameters (ice-shelf thickness and subice-shelf cavity water depth) on the flexural gravity waves propagating through the ice-shelf/subice-shelf cavity system. Analysis of a simplified system—a one-dimensional thin-beam treatment of the ice-shelf flexure coupled with shallow-water treatment of the wave propagation in the cavity—shows that the propagation of the flexural gravity waves, their dispersion relationship, phase and group velocities are determined by the ice-shelf flexural rigidity, which is determined by the ice-shelf thickness and elastic parameters, and the water-column depth of the subice-shelf cavity. The dispersion relationship of the flexural gravity waves can be expressed as a combination of the characteristics of a shallow wave propagating through an open ocean with the depth the same as the subice-shelf cavity water-column thickness and a buoyancy-forced ice-shelf flexural wave (equation (25)).

This dispersion relationship and consequently expressions for the group and phase velocity are valid for the two-dimensional (plan view) geometry as well. The derived expressions for velocities of the flexural gravity waves (inferred from passive seismometer observations) can be used to constrain poorly known Young's modulus. If for instance, group velocities are known for two frequencies,  $\omega_1$  and  $\omega_2$  at a given location, then Young's modulus,  $E$ , can be estimated from the following expression:

$$E = \frac{3(1-\nu^2)\rho_w g^3 H^2}{H_f^3} \frac{\Lambda_p^2 - 1}{\omega_1^4 - \Lambda_p \omega_2^4}, \quad (44)$$

where  $\Lambda_p = \frac{V_p(\omega_1)}{V_p(\omega_2)}$  and  $V_p$  is the flexural gravity wave phase velocity defined by equation (27b). Such observationally constrained estimates of ice Young's modulus can provide a general idea about its spatial and temporal variability.



Results of a three-dimensional numerical model simulating propagation of flexural gravity waves applied to realistic geometry of the Ross Ice Shelf reveal that the waves propagate as narrow beams, whose direction is determined by the direction of incident ocean waves and the width is determined by the frequency of the incident ocean waves—higher frequency incident waves result in narrower beams of the flexural gravity waves. The beam-like structures seem to collocate with areas of large gradients of the cavity water depth. For the considered RIS cavity geometry (Bedmap 2 data set), these areas are primarily determined by the gradients of the ice-shelf draft, due to poor knowledge of the bathymetry of the RIS cavity.

The computed flexural stresses resemble spatial distributions of the beam-like vertical displacement spatial patterns. They have larger magnitudes in areas of the high spatial gradients of the cavity water depth, including shoaling around Roosevelt Island and in the vicinity of the grounding line. They also have larger magnitudes if excited by higher frequency ocean waves. The higher and lower frequency waves have stronger effects at different locations. The lower frequency waves can propagate farther through the RIS/cavity system and produce higher magnitude flexural stresses near the grounding line. In contrast, higher frequency waves produce larger flexural stresses closer to the RIS front, and have smaller effects on areas near the grounding line.

The ice shelf experiences flexural stresses through its whole depth, including vertical shear. The computed magnitudes are on the order of 5–15 kPa, and are smaller than the background stresses associated with the viscous flow of the ice shelf. However, in this flow, the vertical stresses are negligible and the presence of the vertical shear associated with the flexural bending could potentially contribute to initiation of new and development of already existing fractures. Also, the constant impact of the ocean waves, and their cyclic nature, implies that the flexural stresses always contribute to the ice-shelf stress regime.

In contrast to an ice-shelf viscous deformation that has been extensively studied, the ice-shelf flexural behavior, especially its three-dimensional aspects, is still poorly understood. As the presented analysis shows, investigations of the ice-shelf flexural gravity waves can be useful to infer poorly known characteristics of ice shelves. The propagation of the flexural gravity waves as beams observed in the numerical simulations suggests that they could produce spatially concentrated flexural stresses, and consequently, they could contribute to initiation and propagation of the fractures and crevasses. The contributions of the flexural stresses to the overall ice-shelf stress regime can be substantial for thinner ice shelves with shallower water column in their cavities than the Ross Ice Shelf ones considered here. Assessments of flexural stresses and stability of such ice shelves requires further analysis and accurate knowledge of their geometry and especially bathymetry of their cavities.

# Acknowledgments

This study is supported by the U.S. National Science Foundation grant OPP-1246151 and by NOAA grant NA13OAR431009. I thank Doug MacAyeal for fruitful discussions and help with the manuscript, and an anonymous reviewer for thoughtful comments and useful suggestions. The model outputs will be available at National Snow and Ice Data Center [www.nsidc.org](http://www.nsidc.org).

# References

- Bromirski, P., O. V. Sergienko, and D. R. MacAyeal (2010), Transoceanic infragravity waves impacting Antarctic ice shelves, *Geophys. Res. Lett.*, *37*, L02502, doi:10.1029/2009GL041488.
- Bromirski, P. D., A. Diez, P. Gerstoft, R. A. Stephen, T. Bolmer, D. A. Wiens, R. C. Aster, and A. Nyblade (2015), Ross ice shelf vibrations, *Geophys. Res. Lett.*, *42*, 7589–7597, doi:10.1002/2015GL065284.
- Brunt, K. M., and D. R. MacAyeal (2014), Tidal modulation of ice-shelf flow: A viscous model of the Ross Ice Shelf, *J. Glaciol.*, *60*(221), 500–508, doi:10.3189/2012JoG13J203.
- Brunt, K. M., H. A. Fricker, L. Padman, T. A. Scambos, and S. Ortel (2010), Mapping the grounding zone of the Ross Ice Shelf, Antarctica, using ICESat laser altimetry, *Ann. Glaciol.*, *51*(55), 785–788.
- Cathles, L. M., E. A. Okal, and D. R. MacAyeal (2009), Seismic observations of sea swell on the floating Ross Ice Shelf, Antarctica, *J. Geophys. Res.*, *114*, F02015, doi:10.1029/2007JF000934.
- Didenkulova, I., E. Pelinovsky, and T. Soomere (2009), Long surface wave dynamics along a convex bottom, *J. Geophys. Res.*, *114*, C07006, doi:10.1029/2008JC005027.
- Fretwell, P., et al. (2013), Bedmap2: Improved ice bed, surface and thickness datasets for Antarctica, *The Cryosphere*, *7*, 375–393, doi:10.5194/tc-7-375-2013.
- Godin, O. A., and N. A. Zabolot (2016), Resonance vibrations of the Ross ice shelf and observations of persistent atmospheric waves, *J. Geophys. Res. Space Phys.*, *121*, 10,157–10,171, doi:10.1002/2016JA023226.
- Haran, T., J. Bohlander, T. Scambos, and M. Fahnestock (2005), *MODIS Mosaic of Antarctica (MOA) Image Map*, Natl. Snow and Ice Data Cent., Boulder, Colo., doi:10.7265/N5ZK5DM5.
- Holdsworth, G., and J. Glynn (1978), Iceberg calving from floating glaciers by a vibrating mechanism, *Nature*, *274*, 464–466.
- Holdsworth, G., and J. E. Glynn (1981), A mechanism for the formation of large icebergs, *J. Geophys. Res.*, *86*, 3210–3222.
- Longuet-Higgins, M., and R. W. Stewart (1962), Radiation stress and mass transport in gravity waves, with application to “surf beats”, *J. Fluid Mech.*, *13*(4), 481–504, doi:10.1017/S0022112062000877.
- MacAyeal, D., R. A. Bindschadler, S. S. Shabtaie, and C. R. Bentley (1987), Paleothermometry by control methods, *J. Glaciol.*, *33*, 218–230.
- MacAyeal, D. R., and O. V. Sergienko (2013), The flexural dynamics of melting ice shelves, *Ann. Glaciol.*, *54*(63), 1–10, doi:10.3189/2013AoG63A256.

- MacAyeal, D. R., et al. (2006), Transoceanic wave propagation links iceberg calving margins of Antarctica with storms in tropics and Northern Hemisphere, *Geophys. Res. Lett.*, **33**, L17502, doi:10.1029/2006GL027235.
- Maxwell, J. C. (1867), On the dynamical theory of gases, *Philos. Trans. R. Soc. London A*, **157**, 49–88, doi:10.1098/rstl.1987.0004.
- Sergienko, O. V. (2005), Surface melting on ice shelves and icebergs, PhD thesis, Univ. of Chicago, Chicago, Ill.
- Sergienko, O. V. (2010), Elastic response of floating glacier ice to impact of long-period Ocean waves, *J. Geophys. Res.*, **115**, F04028, doi:10.1029/2010JF001721.
- Sergienko, O. V. (2013), Normal modes of a coupled ice-shelf/sub-ice-shelf cavity system, *J. Glaciol.*, **59**(213), 76–80, doi:10.3189/2013JoG12J096.
- Shepherd, A., and N. R. Peacock (2003), Ice shelf tidal motion derived from ERS altimetry, *J. Geophys. Res.*, **108**(C6), 3198, doi:10.1029/2001JC001152.
- Stephenson, S. N. (1984), Glacier flexure and the position of grounding lines—Measurements by tiltmeter on Rutford Ice Stream, Antarctica, *Ann. Glaciol.*, **5**, 165–169.
- Stoker, J. J. (1957), *Water Waves. The Mathematical Theory With Applications, Pure and Applied Mathematics*, vol. 4, 567 pp., Interscience, New York.
- Timoshenko, S. P., and J. N. Goodier (1970), *Theory of Elasticity*, 3rd ed., 567 pp., McGraw-Hill, New York.
- Van der Veen, C. J. (1999), *Fundamentals of Glacier Dynamics*, 1st ed., 472 pp., Taylor and Francis, Rotterdam.
- Vaughan, D. (1995), Tidal flexure at ice shelf margins, *J. Geophys. Res.*, **100**, 6213–6224.